

# Journal of Mechanics of Materials and Structures

**STRESS AND DISPLACEMENT ANALYSIS OF AN AUXETIC QUARTER-PLANE  
UNDER A CONCENTRATED FORCE**

Paweł Fritzkowski and Henryk Kamiński

**Volume 11, No. 1**

**January 2016**



# STRESS AND DISPLACEMENT ANALYSIS OF AN AUXETIC QUARTER-PLANE UNDER A CONCENTRATED FORCE

PAWEŁ FRITZKOWSKI AND HENRYK KAMIŃSKI

The problem of a quarter-space under distributed normal and shear loads is considered. A mathematical model is formulated for the plane strain state. Theoretical background of the Mellin integral transform and calculation of residues is outlined. An analytical procedure involving the Mellin transform is presented for the general reduced problem of a quarter-plane. Numerical computation of residues allows for evaluation of the inverse transforms for the displacements and stresses. Simulation results are obtained for a special load case: a concentrated force. The deformation of the loaded boundary is analyzed for various values of Poisson's ratio. It turns out that auxetics exhibit locally negative stiffness, which leads to an anomalous behavior of the system. A simple explanation of the unusual deformation mechanism is proposed. The semianalytical solutions are compared with the results obtained by means of the finite element method.

## 1. Introduction

In the framework of the classical elasticity theory, a number of fundamental problems have been formulated in unbounded domains such as infinite or semi-infinite space. Prominent examples of this kind are the Boussinesq and the Cerruti problems: an elastic half-space under a normal or tangent concentrated force, respectively [Sadd 2005; Saada 1993; Nowacki 1970]. Usually the specific domain character enables one to apply certain analytical procedures like the complex variable method or the integral transform method (e.g., Laplace or Fourier transform), which can lead to closed-form solutions. Very often it requires considerable model simplifications, e.g., by using the plane stress or plane strain assumption. Nevertheless, such theoretical studies still provide significant information about more practical problems related to, among others, fracture and contact mechanics [Sadd 2005; Saada 1993; Timoshenko and Goodier 1951; Johnson 1985].

Nowadays, in the era of modern computational tools, mostly based on the finite element method, the classical elasticity problems and analytical approaches seem to be of less importance. However, they remain a helpful means of preliminary studies of unconventional systems whose anomalous behavior goes beyond the well-known theoretical solutions. One such example is auxetics, i.e., materials with negative Poisson's ratio,  $\nu < 0$ . Indeed, for decades scientists and researchers have been mainly focusing on traditional engineering materials for which usually  $0.25 < \nu < 0.35$ . But even today, despite numerous present and potential applications of auxetics (e.g., in aerospace, biomedical and military engineering), and constantly developed techniques for their manufacture [Prawoto 2012; Alderson and Alderson 2007], the behavior and mechanical properties of these materials are not intuitive. Therefore, the authors of

---

This work has been supported by grant 02/21/DSPB/3453.

*Keywords:* linear elasticity, quarter-plane, deformation, auxetic materials, Mellin transform.

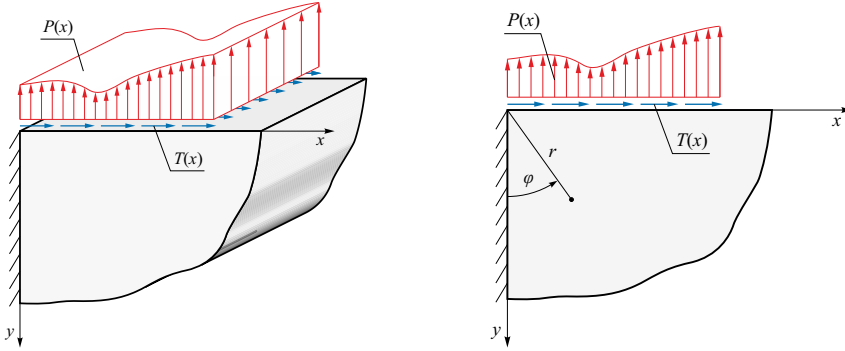


**Figure 1.** Elastic quarter-space with a loaded surface: (left) the primary, three-dimensional problem and (right) the reduced problem of a quarter-plane.

excellent review papers not only report auxetics-related advances in research and technology but also thoroughly discuss the concept and physical significance of Poisson's ratio [Greaves et al. 2011] as well as deformation mechanisms of auxetic systems [Evans and Alderson 2000; Prawoto 2012]. It should be noted that the classical theory of elasticity places the following bounds on Poisson's ratio of isotropic materials [Sadd 2005; Greaves et al. 2011]:  $-1 < \nu < 1/2$ .

This paper is devoted to stress and deformation analysis of an elastic solid quarter-space subjected to a line-distributed loading. Due to the plane strain state, the problem is reduced to a static analysis of a quarter-plane under a concentrated force. A semianalytical approach is used to solve the displacement field equations. More precisely, the Mellin transform technique is applied in combination with a numerical calculation of residues. The main aim of this work is to investigate the effect of Poisson's ratio on deformation of the loaded surface and report on an application of the Mellin transform that has been rather rarely employed in computational practice.

The paper is divided into six sections. In Section 2, a mathematical formulation of the problem is presented. Section 3 outlines the concept of the Mellin integral transform and computation of residues. In turn, a general solution procedure of the stated problem is specified in Section 4. Section 5 contains simulation results and discussion. Conclusions and final remarks are given in Section 6.

## 2. Formulation of the problem

Let us consider the generalized problem of an elastic quarter-space shown in Figure 1, left. The vertical boundary half-plane is fixed, while the horizontal one is free and subjected to distributed normal and shear loads:  $P(x)$  and  $T(x)$ , respectively. The solid material occupying the domain is assumed to be homogeneous, isotropic and linear, and it is characterized by shear modulus  $G$  and Poisson's ratio  $\nu$ . In the case of auxetics,  $\nu < 0$ .

Since the support and loading conditions are independent of the  $z$  coordinate, the spatial problem can be reduced to two dimensions (see Figure 1, right). Accordingly, the plane strain formulation is used below. Now, we focus on a quarter-plane, i.e., the region with semi-infinite boundaries:

$$\Omega = \begin{cases} 0 \leq x < \infty, \\ 0 \leq y < \infty. \end{cases} \quad (2-1)$$

It can be actually treated as a domain in the shape of a right-angle infinite wedge. Therefore, the mathematical model is formulated in a polar coordinate system  $(r, \varphi)$ .

Let  $\mathbf{u}(r, \varphi) = [u_r, u_\varphi]^T$  be the displacement vector, where  $u_r$  and  $u_\varphi$  denote its radial and tangential components. The strain-displacement relations involving only the in-plane strains have the forms

$$\varepsilon_r = \frac{\partial u_r}{\partial r}, \quad \varepsilon_\varphi = \frac{1}{r} \left( u_r + \frac{\partial u_\varphi}{\partial \varphi} \right), \quad \varepsilon_{r\varphi} = \frac{1}{2} \left( \frac{1}{r} \frac{\partial u_r}{\partial \varphi} + \frac{\partial u_\varphi}{\partial r} - \frac{u_\varphi}{r} \right). \quad (2-2)$$

From Hooke's law, the corresponding stress components are given by

$$\sigma_r = \lambda(\varepsilon_r + \varepsilon_\varphi) + 2\mu\varepsilon_r, \quad \sigma_\varphi = \lambda(\varepsilon_r + \varepsilon_\varphi) + 2\mu\varepsilon_\varphi, \quad \sigma_{r\varphi} = 2\mu\varepsilon_{r\varphi}, \quad (2-3)$$

where  $\lambda$  and  $\mu$  are Lamé constants:

$$\lambda = \frac{2G\nu}{1-2\nu}, \quad \mu = G. \quad (2-4)$$

Finally, in the case of zero body forces, the Navier–Lamé equations reduce to [Nowacki 1970; Sadd 2005]

$$\mu \left( \nabla^2 u_r - \frac{u_r}{r^2} - \frac{2}{r^2} \frac{\partial u_\varphi}{\partial \varphi} \right) + (\lambda + \mu) \frac{\partial}{\partial r} \left( \frac{1}{r} \frac{\partial}{\partial r} (r u_r) + \frac{1}{r} \frac{\partial u_\varphi}{\partial \varphi} (r u_r) \right) = 0, \quad (2-5a)$$

$$\mu \left( \nabla^2 u_\varphi - \frac{u_\varphi}{r^2} - \frac{2}{r^2} \frac{\partial u_r}{\partial \varphi} \right) + (\lambda + \mu) \frac{1}{r} \frac{\partial}{\partial \varphi} \left( \frac{1}{r} \frac{\partial}{\partial r} (r u_r) + \frac{1}{r} \frac{\partial u_\varphi}{\partial \varphi} (r u_r) \right) = 0. \quad (2-5b)$$

Moreover, for the given quarter-plane problem, the unknown vector-valued function  $\mathbf{u}(r, \varphi)$  must satisfy the following mixed boundary conditions:

$$u_r(r, 0) = u_\varphi(r, 0) = 0 \quad (\text{displacement conditions}), \quad (2-6a)$$

$$\sigma_\varphi(r, \pi/2) = P(r) \quad (\text{traction condition}), \quad (2-6b)$$

$$\sigma_{r\varphi}(r, \pi/2) = T(r) \quad (\text{traction condition}). \quad (2-6c)$$

Thus, the resulting mathematical model consists of the system of coupled partial differential equations (2-5) together with four boundary conditions (2-6).

The boundary value problem is not of a simple nature. To solve it analytically, we apply operational calculus with the Mellin transformation method. Owing to the fact that this mathematical tool is less commonly used than other integral transforms (e.g., the Fourier or Laplace transforms), basic theoretical concepts are outlined in the next section.

### 3. Mathematical background

In literature one can find a few applications of the classical Mellin transform to plane elasticity problems. Sneddon [1951] considered an infinite elastic wedge subjected to surface stresses. Consequently, the author used the stress formulation and an Airy stress function. A similar approach for a finite wedge was employed by Tsamasphyros and Theocaris [1979]. They obtained the stress function as an asymptotic expansion of the complex inversion integral. More recently, Martin [2003] analyzed the problem of a composite elastic half-plane, made from two isotropic quarter-planes, subjected to a concentrated force. An exact solution was constructed using Mellin transforms and the Melan solution for a homogeneous

half-plane. Moreover, the Mellin transform was applied to some fracture and contact problems for wedge-shaped domains; see, e.g., [Erdogan and Arin 1976; Theocaris and Makrakis 1987]. In these cases, understandably, the stress formulation was preferable too.

The information given below is a concise selection from many handbooks devoted to both mathematical theory and applications. The interested reader is referred especially to [Kącki 1992; Bateman 1954; Debnath and Bhatta 2007].

Let  $f(x)$  be a function of a real variable  $x$ . The Mellin integral transform of  $f$  is defined by

$$\tilde{f}(s) = \int_0^{\infty} f(x)x^{s-1} dx, \quad (3-1)$$

where  $s$  is a complex variable. In further considerations, the transform will be denoted symbolically by

$$\tilde{f}(s) = \mathcal{M}[f(x)]. \quad (3-2)$$

The inverse Mellin transform, in turn, is defined formally as

$$f(x) = \mathcal{M}^{-1}[\tilde{f}(s)] = \frac{1}{2\pi i} \int_{c-i\infty}^{c+i\infty} \tilde{f}(s)x^{-s} ds, \quad (3-3)$$

where  $i$  is the imaginary unit and  $c$  lies on the complex plane in the strip of analyticity of the function  $\tilde{f}(s)$ .

Additionally, for further purposes, two operational properties of the Mellin transform are listed below:

- Suppose that  $\tilde{f}(s)$  is defined by (3-2) and there exists the Mellin transform of

$$g(x) = \left(x \frac{d}{dx}\right)^n f(x). \quad (3-4)$$

Then

$$\mathcal{M}[g(x)] = (-s)^n \tilde{f}(s). \quad (3-5)$$

- Let  $f(x, y)$  be a function of two variables. If

$$\mathcal{M}_x[f(x, y)] = \tilde{f}(s, y) \quad (3-6)$$

is the Mellin transform of  $f$  with respect to  $x$ , then

$$\mathcal{M}_x \left[ \frac{\partial^n f(x, y)}{\partial y^n} \right] = \frac{\partial^n \tilde{f}(s, y)}{\partial y^n}. \quad (3-7)$$

Suppose that  $f(x)$  is an unknown solution of a given problem. Moreover, let  $g(s) = \tilde{f}(s)$  be its Mellin transform, i.e., the solution of the problem transformed by means of the direct transformation. Obviously, the inverse Mellin transform is used to recover  $f$  from  $g$ . In practice, the complex integral (3-3) can be calculated by applying Cauchy's residue theorem. Accordingly, if  $D$  is a region bounded by a simple closed contour  $C$  and  $g(s)$  is analytic in  $D$ , except for a finite number of isolated singularities at  $s_1, s_2, \dots, s_n$ , then the counterclockwise contour integral

$$\oint_C g(s) ds = 2\pi i \sum_{k=1}^n \text{Res}[g(s), s_k], \quad (3-8)$$

where  $\text{Res}[g(s), s_k]$  denotes the residue of  $g(s)$  at  $s_k$  [Bronsztejn et al. 2009; Kaplan 2002].

As can be seen, calculating residues of the direct transform is crucial to an efficient evaluation of the inverse transform. In particular, the following rule is indispensable in computational practice: if  $g(s)$  is a function of the form

$$g(s) = \frac{p(s)}{q(s)} \quad (3-9)$$

and it has a pole of first order at  $s_0$ , then

$$\text{Res}[g(s), s_0] = \frac{p(s_0)}{q'(s_0)}. \quad (3-10)$$

The outlined Mellin transform method together with a numerical computation of residues allow for a semianalytical treatment of the quarter-plane problem, which is discussed in the next sections.

#### 4. General analytical procedure

**4A. Transformation of the problem.** Let  $\tilde{u}_r$  and  $\tilde{u}_\varphi$  denote the Mellin transforms of the displacements with respect to the polar coordinate  $r$ , that is,

$$\tilde{u}_r(s, \varphi) = \mathcal{M}_r[u_r(r, \varphi)], \quad \tilde{u}_\varphi(s, \varphi) = \mathcal{M}_r[u_\varphi(r, \varphi)]. \quad (4-1)$$

Multiplying the governing equations (2-5) by  $r^2$  and using the properties (3-5) and (3-7) yields the following transformed pair:

$$\mu \frac{\partial^2 \tilde{u}_r}{\partial \varphi^2} + (\lambda + 2\mu)(s^2 - 1)\tilde{u}_r - [s(\lambda + \mu) + (\lambda + 3\mu)] \frac{\partial \tilde{u}_\varphi}{\partial \varphi} = 0, \quad (4-2a)$$

$$(\lambda + 2\mu) \frac{\partial^2 \tilde{u}_\varphi}{\partial \varphi^2} + \mu(s^2 - 1)\tilde{u}_\varphi - [s(\lambda + \mu) - (\lambda + 3\mu)] \frac{\partial \tilde{u}_r}{\partial \varphi} = 0. \quad (4-2b)$$

It should be noted that these equations are much simpler than the original ones.

Next, consider the stress-displacement relations that can be obtained by inserting (2-2) into (2-3). Transformations of the stress components multiplied by  $r$

$$\tilde{t}_r(s, \varphi) = \mathcal{M}_r[r\sigma_r(r, \varphi)],$$

$$\tilde{t}_\varphi(s, \varphi) = \mathcal{M}_r[r\sigma_\varphi(r, \varphi)],$$

$$\tilde{t}_{r\varphi}(s, \varphi) = \mathcal{M}_r[r\sigma_{r\varphi}(r, \varphi)]$$

become

$$\tilde{t}_r(s, \varphi) = [\lambda - s(\lambda + 2\mu)]\tilde{u}_r + \lambda \frac{\partial \tilde{u}_\varphi}{\partial \varphi}, \quad (4-3a)$$

$$\tilde{t}_\varphi(s, \varphi) = [(\lambda + 2\mu) - s\lambda]\tilde{u}_r + (\lambda + 2\mu) \frac{\partial \tilde{u}_\varphi}{\partial \varphi}, \quad (4-3b)$$

$$\tilde{t}_{r\varphi}(s, \varphi) = \mu \left[ -(s + 1)\tilde{u}_\varphi + \frac{\partial \tilde{u}_r}{\partial \varphi} \right]. \quad (4-3c)$$

Now, boundary conditions (2-6) can be converted to

$$\tilde{u}_r(s, 0) = \tilde{u}_\varphi(s, 0) = 0 \quad (\text{displacement conditions}), \quad (4-4a)$$

$$\tilde{t}_\varphi(s, \pi/2) = \tilde{P}(s) \quad (\text{traction condition}), \quad (4-4b)$$

$$\tilde{t}_r\varphi(s, \pi/2) = \tilde{T}(s) \quad (\text{traction condition}), \quad (4-4c)$$

where

$$\tilde{T}(s) = \mathcal{M}_r[rT(r)], \quad \tilde{P}(s) = \mathcal{M}_r[rP(r)]. \quad (4-5)$$

To sum up, after the transformation the boundary value problem comprises the equilibrium equations (4-2) and associated boundary conditions (4-4).

**4B. Solution of the problem.** Due to its relatively simple form, the transformed problem can be solved in a quite conventional way. For the second-order partial differential equations (4-2), one can suppose that

$$\tilde{u}_r(s, \varphi) = C_1 e^{h\varphi}, \quad \tilde{u}_\varphi(s, \varphi) = C_2 e^{h\varphi}, \quad (4-6)$$

where  $C_1$  and  $C_2$  are real constants, while  $h$  is a complex parameter to be determined. Inserting (4-6) into (4-2) leads to a system of two characteristic equations. All their roots are complex:

$$h_1 = i(s+1), \quad h_2 = -i(s+1), \quad h_3 = i(s-1), \quad h_4 = -i(s-1).$$

Hence, the solution is given by

$$\tilde{u}_r(s, \varphi) = A_{11} \sin[(s+1)\varphi] + B_{11} \cos[(s+1)\varphi] + A_{12} \sin[(s-1)\varphi] + B_{12} \cos[(s-1)\varphi], \quad (4-7a)$$

$$\tilde{u}_\varphi(s, \varphi) = A_{21} \sin[(s+1)\varphi] + B_{21} \cos[(s+1)\varphi] + A_{22} \sin[(s-1)\varphi] + B_{22} \cos[(s-1)\varphi], \quad (4-7b)$$

where  $A_{11}, B_{11}, A_{12}, \dots, A_{22}$  are real constants. As can be ascertained by substitution, in order to satisfy (4-2), the relations

$$A_{21} = B_{11} \frac{\eta_1 s - \eta_3}{\eta_1 s + \eta_3}, \quad A_{22} = B_{12}, \quad B_{21} = -A_{11} \frac{\eta_1 s - \eta_3}{\eta_1 s + \eta_3}, \quad B_{22} = -A_{12} \quad (4-8)$$

must be fulfilled, where auxiliary parameters are introduced for notational brevity:

$$\eta_j = \lambda + j\mu, \quad j = 1, 2, 3.$$

The next four constants can be determined from the prescribed boundary conditions. Taking into consideration (4-4a) produces

$$B_{12} = -B_{11}, \quad A_{12} = -A_{11} \frac{\eta_1 s - \eta_3}{\eta_1 s + \eta_3}. \quad (4-9)$$

Similarly, the traction conditions (4-4b) and (4-4c) require

$$A_{11} = -\frac{\tilde{T}(\eta_1 s + \eta_3) + 4B_{11}\mu s(\eta_1 s + \eta_2) \cos(\frac{1}{2}\pi s)}{4\mu s(\eta_1 s - \mu) \sin(\frac{1}{2}\pi s)}, \quad (4-10)$$

$$B_{11} = -\frac{(\eta_1 s + \eta_3) [\tilde{P}(\eta_1 s - \mu) \sin(\frac{1}{2}\pi s) + \tilde{T}(\eta_1 s + \eta_2) \cos(\frac{1}{2}\pi s)]}{2\mu s [2(\eta_1^2 s^2 - \mu^2) - \eta_1 \eta_3 \cos(\pi s) - \eta_1 \eta_3]}.$$

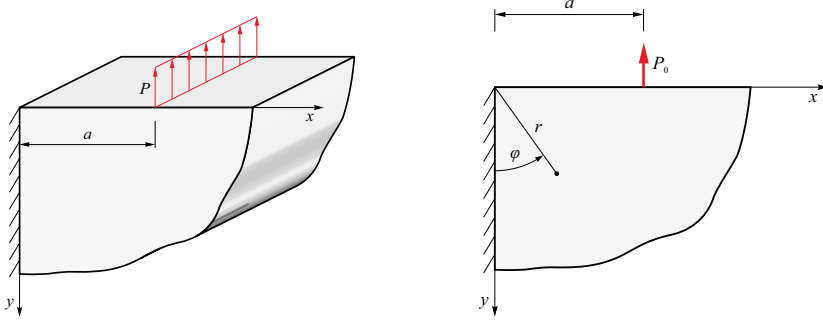


**Figure 2.** Elastic quarter-space with line-distributed loading: (left) the primary, three-dimensional problem and (right) the reduced problem of a quarter-plane under a concentrated force.

Using all the relationships (4-8), (4-9) and (4-10), one can find expressions for the Mellin transforms of the desired displacement, strain and stress components. They are not presented here because of their considerable complexity. Instead, we concentrate on displacements related to the loaded boundary:

$$\tilde{u}_r(s, \pi/2) = \frac{\tilde{T}}{2Gq(s)} \kappa(\kappa + 1) \sin(\pi s) - \frac{\tilde{P}}{2Gq(s)} [4s^2 + 2(\kappa + 1)s + \kappa(\kappa - 1)(\cos(\pi s) - 1)], \quad (4-11a)$$

$$\tilde{u}_\varphi(s, \pi/2) = \frac{\tilde{P}}{2Gq(s)} \kappa(\kappa + 1) \sin(\pi s) + \frac{\tilde{T}}{2Gq(s)} [4s^2 - 2(\kappa + 1)s + \kappa(\kappa - 1)(\cos(\pi s) - 1)], \quad (4-11b)$$

where  $\kappa$  denotes the Kolosov constant

$$\kappa = 3 - 4\nu \quad (4-12)$$

and the common variable part of the denominators is

$$q(s) = s[1 - 4s^2 + \kappa^2 + 2\kappa \cos(\pi s)]. \quad (4-13)$$

For a certain load case, the obtained formulas can be subjected to the inverse Mellin transform performed numerically, which leads to displacement values  $u_r$  and  $u_\varphi$ .

## 5. Case study and results

**5A. Analytical results.** Consider the specific problem indicated in the title. The original problem relates to an elastic quarter-space with a line load that is applied at a distance  $a$  from the  $z$  axis (see Figure 2, left). Consequently, in the plain strain formulation, the horizontal edge of the quarter-plane is loaded by a concentrated force  $P_0$ . Thus,

$$P(r) = P_0 \delta(r - a), \quad T(r) = 0,$$

where  $\delta$  denotes the Dirac delta. Then the boundary conditions (2-6) become

$$u_r(r, 0) = u_\varphi(r, 0) = 0 \quad (\text{displacement conditions}), \quad (5-1a)$$

$$\sigma_\varphi(r, \pi/2) = P_0 \delta(r - a) \quad (\text{traction condition}), \quad (5-1b)$$

$$\sigma_{r\varphi}(r, \pi/2) = 0 \quad (\text{traction condition}). \quad (5-1c)$$



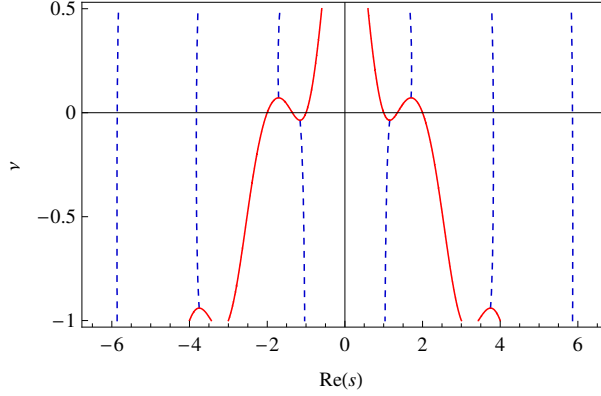


**Figure 3.** Values of the real parts of poles versus Poisson's ratio: real poles (solid) and initial complex poles (dashed).

The nonhomogeneous traction condition can be easily transformed by using the so-called sifting property of the Dirac delta:

$$\tilde{P}(s) = \int_0^\infty r P(r) r^{s-1} dr = \int_0^\infty r^s P_0 \delta(r-a) dr = P_0 a^s.$$

Taking into account that  $\tilde{T}(s) = 0$ , the complete set of transformed conditions (4-4) is given by

$$\tilde{u}_r(s, 0) = \tilde{u}_\varphi(s, 0) = 0 \quad (\text{displacement conditions}), \quad (5-2a)$$

$$\tilde{t}_\varphi(s, \pi/2) = P_0 a^s \quad (\text{traction condition}), \quad (5-2b)$$

$$\tilde{t}_r(s, \pi/2) = 0 \quad (\text{traction condition}). \quad (5-2c)$$

By analogy to the general case, we present only the Mellin transforms of displacements of the loaded surface. Equations (4-11) become

$$\tilde{u}_r(s, \pi/2) = -\frac{P_0 a^s}{2Gq(s)} [4s^2 + 2(\kappa + 1)s + \kappa(\kappa - 1)(\cos(\pi s) - 1)], \quad (5-3a)$$

$$\tilde{u}_\varphi(s, \pi/2) = \frac{P_0 a^s}{2Gq(s)} \kappa(\kappa + 1) \sin(\pi s). \quad (5-3b)$$

Expressions for  $\tilde{t}_r$ ,  $\tilde{t}_\varphi$  and  $\tilde{t}_{r\varphi}$  are much more complex; however, they also include the denominator  $q(s)$ .

**5B. Some computational issues.** As suggested in Section 3, the inversion process can be performed via numerical evaluation of residues. This approach requires finding poles of the given Mellin transforms multiplied by  $r^{-s}$ . Since the integrands of the inversion integral (3-3) can be written in the form (3-9), the function  $q(s)$  plays a key role. In fact, the solutions of the transcendental equation  $q(s) = 0$  must be found.

It can be easily shown that the integrands do not have poles at  $s = 0$ , whereas the other zeros of  $q(s)$  correspond to the poles of first order. Their location in the complex plane is symmetric with respect to both axes. Figure 3 shows values of the real parts of a few initial poles, calculated for the whole range  $-1 \leq \nu \leq 1/2$ . There is a finite number  $2n_r$  of real poles, all of which lie near the origin ( $1 \leq n_r \leq 3$ ). Moreover, there are infinitely many complex conjugate poles ( $n_c = \infty$ ).

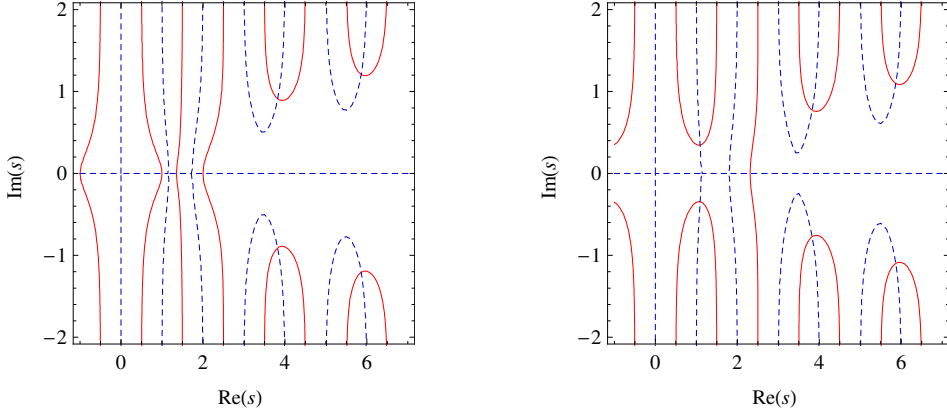


**Figure 4.** Zero-level contour lines of the real part (solid) and the imaginary part (dashed) of  $q(s)$ : (left)  $\nu = 0$  and (right)  $\nu = -0.25$ . The intersections of different contours indicate poles' loci.

Achieving a good insight into the pattern of singularities' locations is essential to construct an algorithm for evaluation of residues. Due to the mentioned symmetry, we concentrate on the right half-plane. In Figure 4 two isoline plots are presented for  $\nu = 0$  and  $\nu = -0.25$ . They display just the zero-level contours of the real and imaginary parts of the function  $q(s)$ . Thus, a real pole  $s_{rk} = \alpha_{rk}$  ( $k = 1, 2, \dots, n_r$ ) of  $p(s)/q(s)$  is indicated by the intersection of a real-part-related contour with the real axis. A complex pole  $s_{ck} = \alpha_{ck} + \beta_{ck}i$  ( $k = 1, 2, \dots, n_c$ ), in turn, lies at the intersection of two contours of different types and has a corresponding conjugate,  $\bar{s}_{ck} = \alpha_{ck} - \beta_{ck}i$ . As  $\nu = 0$ , for example, in the right half-plane three real poles  $s_{r1}$ ,  $s_{r2}$  and  $s_{r3}$  are followed by all the complex poles  $s_{ck}$  and  $\bar{s}_{ck}$  ( $k = 1, 2, \dots, n_c$ ). For the other case, in turn, a single real pole  $s_{r1}$  is located between the first and second complex conjugate pairs,  $s_{c1}$ ,  $\bar{s}_{c1}$  and  $s_{c2}$ ,  $\bar{s}_{c2}$ . Generally, the difference between the real parts of two directly neighboring complex poles  $\Delta\alpha_c = \alpha_{c_{k+1}} - \alpha_{c_k} \approx 2$ , whereas the imaginary difference decreases exponentially to zero ( $\Delta\beta_c \rightarrow 0$ ).

Although there is an infinite number of isolated complex singularities, residue values gradually decrease with increasing absolute value of the real part  $\alpha_{ck}$ . Consequently, the true solution can be well-approximated by a finite (truncated) sum of residues of the direct transforms. The degree of accuracy of this approximation is affected by two factors. Firstly, one should reasonably select the number  $n_c^*$  of the complex poles being taken. Secondly, the numerical solution of  $q(s) = 0$  plays a vital role. In our simulations the real roots are found with the use of Muller's method. The complex roots, in turn, are obtained by a consecutive application of the method of successive approximations (a fixed-point iteration scheme).

In practice, calculation of the so-called Bromwich integral (3-3) may seem a bit enigmatic. The integration must be performed along an infinite line  $L$  that is parallel to the imaginary axis ( $\text{Re}(s) = c$ ). In the given problem, two lines,  $L_1$  and  $L_2$ , are used as illustrated in Figure 5. Thus,  $c_1 = c$  and  $c_2 = -c$  where  $c$  is a small positive value so that  $c < s_{r1}$  as well as  $c < \text{Re}(s_{c1})$ . Additionally, two half-circles of radius  $R$ ,  $\Gamma_1$  and  $\Gamma_2$ , are chosen as the completion paths. For  $R \rightarrow \infty$  the lines and curves constitute closed contours,  $C_1 = L_1 \cup \Gamma_1$  and  $C_2 = L_2 \cup \Gamma_2$ , which enclose all the poles in the right and left complex half-planes, respectively. Convergence of the computation can be ensured by the proper choice of the inversion contour.

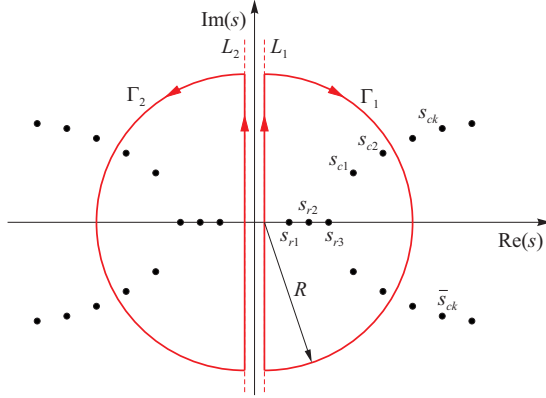


**Figure 5.** Two alternative inversion contours to use in the Bromwich integral.

Generally, the Mellin transforms of the displacements,  $\tilde{u}_r(s, \varphi)$  and  $\tilde{u}_\varphi(s, \varphi)$ , have the form  $\tilde{f}(s, \varphi) = p(s, \varphi)/q(s, \varphi)$ . The integrands for the inversion formula (3-3), in turn, are given by

$$\tilde{f}(s, \varphi)r^{-s} = \left(\frac{r}{a}\right)^{-s} \frac{p^*(s, \varphi)}{q(s, \varphi)}. \quad (5-4)$$

It can be shown that the behavior of these functions is determined by the factor  $(r/a)^{-s}$ . For  $r \geq a$  the functions tend to zero if  $\text{Re}(s) \rightarrow +\infty$ . Thus, the integral of (5-4) along the curve  $\Gamma_1$  vanishes in the limit for  $R \rightarrow \infty$ , and the Bromwich integral can be evaluated by means of the contour  $C_1$ . In the other case, when  $r < a$ , the integrands tend to zero if  $\text{Re}(s) \rightarrow -\infty$ . Consequently, the contour  $C_2$  is used for the inversion integral since the integral along the curve  $\Gamma_2$  vanishes for  $R \rightarrow \infty$ . In both cases, the integration is performed by summing up the residues enclosed by  $C_1$  or  $C_2$ .

**5C. Simulation results.** Although an immanent feature of numerical calculations is that they are performed for specific values of model parameters, the results reported below have a nondimensional form. More precisely, the dimensionless displacements are defined as

$$U_x(x, y) = \frac{Ga}{P_0} u_x(x, y) \times 10^6, \quad U_y(x, y) = \frac{Ga}{P_0} u_y(x, y) \times 10^6. \quad (5-5)$$

The polar components,  $U_r(r, \varphi)$  and  $U_\varphi(r, \varphi)$ , are computed in the same way. Analogously, the following nondimensional stresses are introduced:

$$S_x(x, y) = \frac{a}{P_0} \sigma_x(x, y), \quad S_y(x, y) = \frac{a}{P_0} \sigma_y(x, y), \quad S_{xy}(x, y) = \frac{a}{P_0} \sigma_{xy}(x, y). \quad (5-6)$$

Let us start with an overall look at the displacement and stress fields. Figure 6 shows the distribution of the vertical displacement  $U_y$ , normal stress  $S_y$  and shear stress  $S_{xy}$  in a rectangular subregion of the quarter-plane,  $(0, 2a) \times (0, a)$ , for two values of Poisson's ratio:  $\nu = 0.25$  and  $\nu = -0.5$ . Generally, in both cases the distributions are qualitatively similar, and far away from the fixed boundary, their nature resembles the results for an elastic half-plane (see, e.g., [Sadd 2005; Saada 1993]). The effects of the concentrated force are highly localized. The displacement  $U_y$  decreases radially outward from the point of application of the load. The contours of constant tensile stress  $S_y$  form closed curves converging at

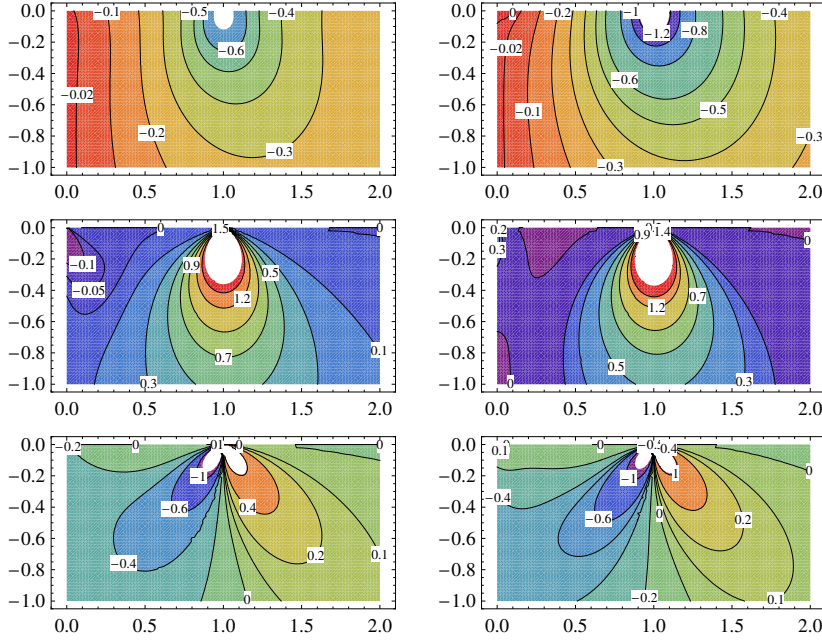


**Figure 6.** Displacement and stress distributions in a rectangular region for  $\nu = 0.25$  (left column) and  $\nu = -0.5$  (right column): (top) vertical displacement  $U_y$ , (middle) normal stress  $S_y$  and (bottom) shear stress  $S_{xy}$ . Results obtained for  $n_c^* = 5 \times 10^3$ .

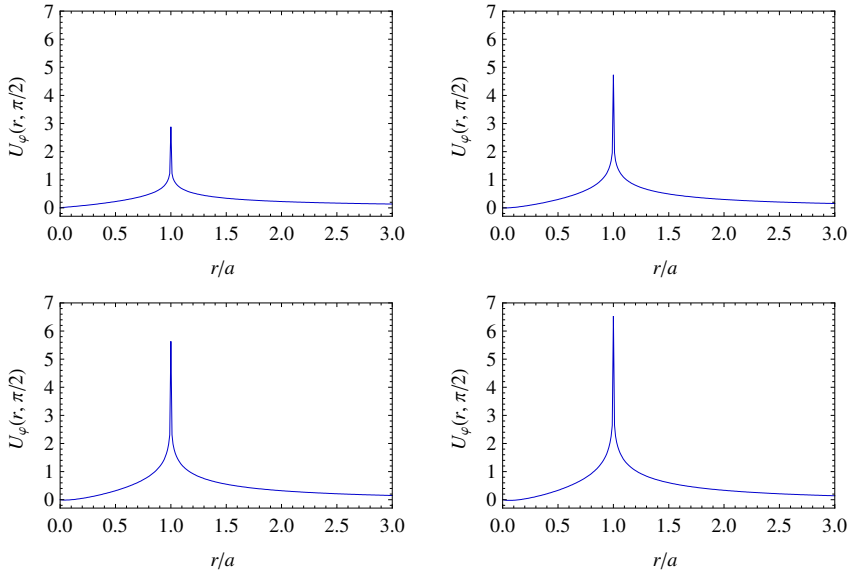


**Figure 7.** Vertical displacement of the loaded surface for various values of Poisson's ratio: (top left)  $\nu = 0.25$ , (top right)  $\nu = -0.25$ , (bottom left)  $\nu = -0.5$  and (bottom right)  $\nu = -0.75$ . Results obtained for  $n_c^* = 3 \times 10^4$ .

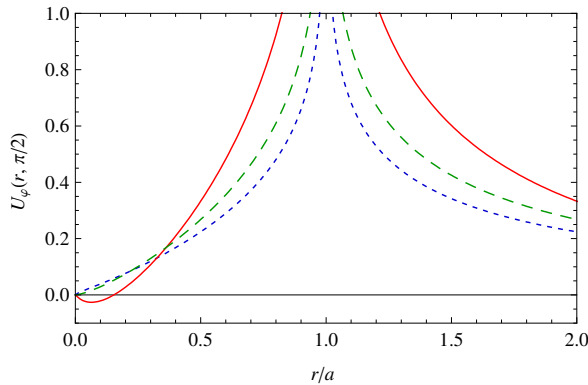


**Figure 8.** The effect of the anomalous vertical displacement of the loaded surface for negative Poisson's ratio:  $\nu = -0.75$  (solid),  $\nu = 0$  (dashed) and  $\nu = 0.25$  (dotted).

this point. In this sense they bring to mind the isochromatic photoelastic fringe patterns (isolines of the principal shear stress) for a point load, well-known from contact mechanics [Sadd 2005; Johnson 1985]. The shear stress field indicates that below the free surface, for example at the level  $y_1 = a/10$ , a change in sign of  $S_{xy}(x, y_1)$  occurs at  $x = a$  (compare the classical Flamant problem [Sadd 2005]). The stress becomes vanishingly small at a sufficiently large distance from this point. Obviously, due to the constraints, the general view is disturbed by some local effects near the fixed boundary, which is discussed later.

Now let us turn to a displacement analysis of the loaded surface. In Figure 7 the vertical displacement  $U_\varphi(r, \pi/2) = -U_y(x, 0)$  is presented for various values of Poisson's ratio. For ease of comparison, all the plots have equal axis scales. As can be seen, values of the sharp peak at the loading point grow with decreasingly lower  $\nu$ . The deformation behavior is intuitively reasonable and seems qualitatively identical in each case. However, a closer look at the curves allows one to notice an interesting detail. If  $\nu > 0$  the vertical displacement component of every point on the boundary is directed upward, i.e., has the same direction as the active force. But for the auxetic case,  $\nu < 0$ , a strict minimum of the function  $U_\varphi(r, \pi/2)$  arises in the range  $0 < r < a$ : the edge deflects locally in the opposite direction to the load. This unusual valley effect can be clearly observed in Figure 8. Zero Poisson's ratio seems to be the intermediate case, when the deflection curve is tangent to the horizontal axis at  $r = 0$ .

Figure 9 shows how Poisson's ratio affects the zero locus  $x_0$  of the function  $-U_y(x, 0)$ . Evidently, the distance between the zero-crossing and the origin increases as  $\nu$  tends to  $-1$ . In the opposite case, when  $\nu = 0$ , the two points overlap, i.e., there is no additional minimum for  $x > 0$ . Thus,  $\nu = 0$  can be treated as the critical value,  $\nu_{cr}$ , below which the valley effect always occurs; the effect intensifies with stronger auxetic behavior exhibited by the material.

In general, mutually opposite directions of the active force and the resulting displacement contradict practical experience. This property is referred to as negative stiffness and should be distinguished from negative Poisson's ratio. However, systems with such an anomaly exist not only in theory. Experimental realization of composite materials with negative stiffness has been discussed, for example, in [Lakes et al. 2001; Lakes 2001].

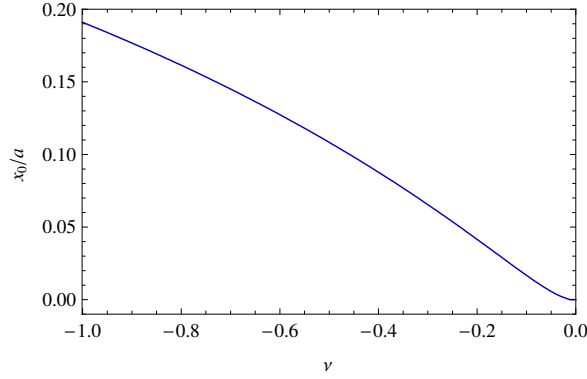


**Figure 9.** Locus of the zero of  $U_\varphi(r, \pi/2)$  versus Poisson's ratio.

In [Maruszewski et al. 2010; Poźniak et al. 2010] it is suggested that the unusual deformation found in our simulations may be treated as locally negative compliance. The authors numerically investigated similar behavior of simple two- or three-dimensional systems. In the planar case, they considered a unit square domain whose two opposite sides are fixed, whereas the others are subjected to uniform compression loading. The elastostatic problem was solved under the plane stress assumption by using the finite element method (FEM). The results indicate counterintuitive deformation of the square near its vertices for negative Poisson's ratio. Nevertheless, the papers do not contain the definite conclusion that  $\nu = 0$  is the critical value for occurrence of this effect. With the FEM approach, the evaluated  $\nu_{\text{cr}}$  strongly depends on the mesh density. Analyzing the result convergence, the authors stated that  $\nu_{\text{cr}} \geq -0.25$  [Poźniak et al. 2010] or  $\nu_{\text{cr}} \geq -0.2$  [Maruszewski et al. 2010].

Finally, the question about the mechanism of the anomalous deformation arises. The contour plots shown in Figure 10 refer to a smaller fragment of the quarter-plane:  $\langle 0, a \rangle \times \langle 0, a \rangle$ . In the left-hand column the distribution of the stress  $S_y$  is presented more clearly than before. The right-hand plots, in turn, display isolines of the first (maximum) principal strain  $\varepsilon_1$ , which is scaled according to

$$E_1 = 2(1 + \nu)G \frac{a^2}{P_0} \varepsilon_1. \quad (5-7)$$

For various values of  $\nu$  both the fields have quite similar character in the area below the load. The most significant differences appear at the fixed edge, near the origin.

When it comes to the normal stress  $S_y$ , there is an evident change in sign due to a decrease of Poisson's ratio. The corner of compressive stress (for  $\nu = 0.25$ ) becomes a neutral zone ( $S_y = 0$ ) with a closed area of low compression (for  $\nu = 0$ ) and is eventually transformed into a corner of tensile stress and a wedge neutral zone at the free surface (for  $\nu = -0.5$ ). In the latter case one should notice the specific saddle-shaped arrangement of the near zero-level contours.

This gradual transformation of the normal stress, among others, entails an essential change in the maximum principal strain  $E_1$ . As  $\nu > 0$ , the material undergoes elongation just under the free surface, which results mainly from the pulling force and the counterdirected reaction. For the critical value,  $\nu = 0$ , the strain  $E_1$  is close to zero at the boundary but still nonnegative in the area below. As  $\nu < 0$ , however,

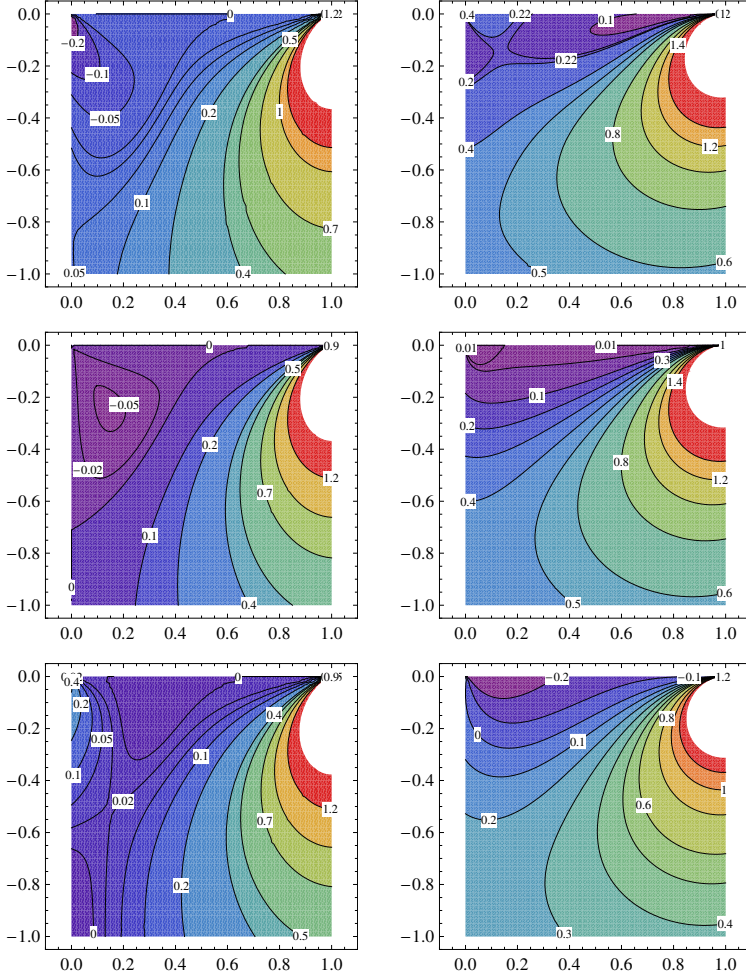


**Figure 10.** Stress and strain distribution in a square region. Normal stress  $S_y$  (left column) and the first principal strain  $E_1$  (right column): (top)  $\nu = 0.25$ , (middle)  $\nu = 0$  and (bottom)  $\nu = -0.5$ .

the maximum strain here becomes negative, and the isolines form a valley that strictly corresponds to the anomalous deformation of the loaded surface.

These differences arising when  $\nu$  is varied may be basically explained by the example of a finite-sized elastic solid under uniaxial tensile load. First, consider the unconstrained case illustrated in Figure 11, left. Typically for conventional (nonauxetic) materials, elongation is accompanied by transverse contraction (see Figure 11, middle). Auxetics, by contrast, expand laterally in the same conditions (see Figure 11, right). Now, suppose that geometric constraints (fixed support) are imposed on the left side of the square. In the normal case ( $\nu > 0$ ), the contraction of the solid generally produces a pulling horizontal (leftward) reaction force. Near the top-left corner, the displacement tendency of the vertex causes a slight pushing (rightward) reaction. As an overall result, the tension zone appears under the free surface. In the auxetic case, in turn, the lateral expansion must generate a pushing (rightward) reaction. The high horizontal

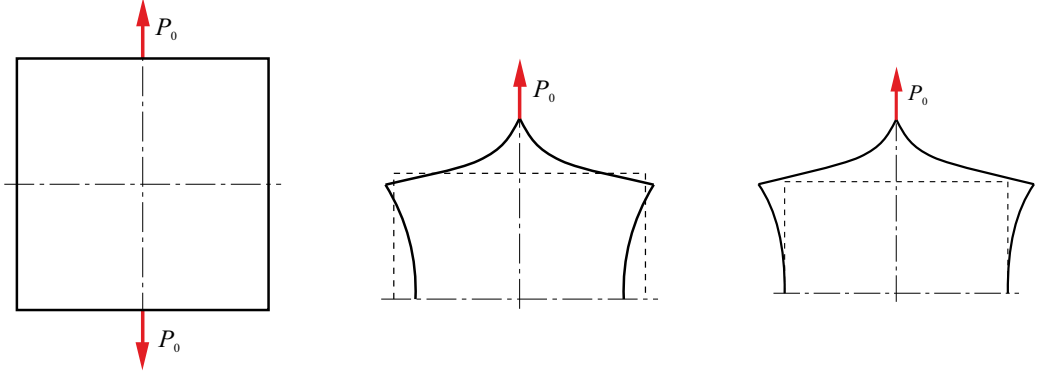


**Figure 11.** Deformation of an unconstrained elastic square under a tensile point load: (left) initial geometry and loading, (middle) deformation scheme in an ordinary, nonauxetic case and (right) deformation scheme in an auxetic case.

compression at the corner may lead to a local contraction in the transverse (vertical) direction, which manifests itself by the valley effect.

Despite its simplicity and schematic nature, the above explanation casts some light on the mechanism of the anomalous deformation of the quarter-plane. To some degree, the expansion-contraction behavior of the conventional and auxetic materials is reflected in the streamline patterns for the displacement field in the system (see Figure 12).

**5D. Comparison to FEM results.** Usually approximate methods are tested and validated by comparing their results to exact solutions. However, another well-established computer method also can be a source of the reference data. Very often the finite element method is employed for this purpose as one of the dominant tools applied in various fields of science and engineering. For instance, FEM results were used to test efficiency of mesh-based and meshless techniques in [Walczak et al. 2014; Bai and Lu 2004; Liu 2010]. Similar comparative study is carried out below for the semianalytical approach. All the presented results have been obtained using the COMSOL Multiphysics environment.

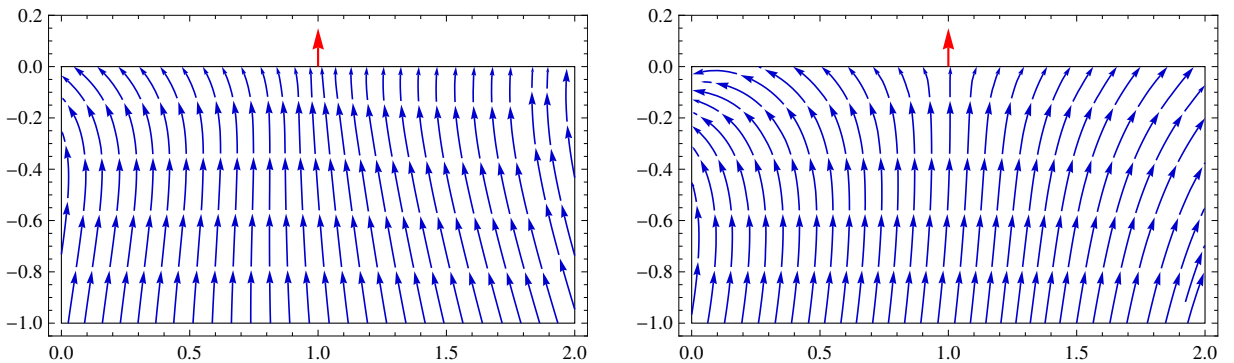


**Figure 12.** Streamline patterns for the displacement field: (left)  $\nu = 0.25$  and (right)  $\nu = -0.5$ .



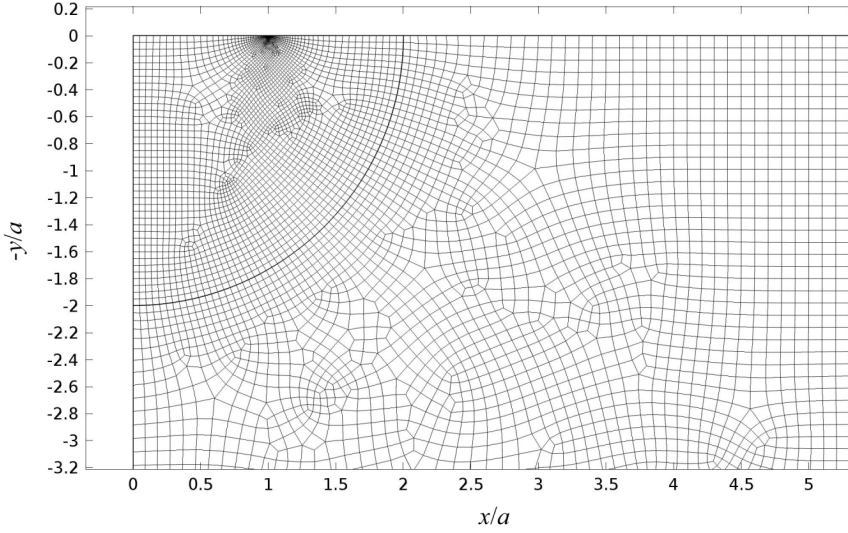


**Figure 13.** Finite element mesh near the loading point (a clipped view).

Some commercial FEM systems offer various implementations of infinite elements, which allows one to model unbounded domains. However, we decided to restrict the linear static analysis to a finite-sized square solid:

$$\widehat{\Omega} = \begin{cases} 0 \leq x \leq b, \\ 0 \leq y \leq b, \end{cases} \quad (5-8)$$

where  $b > a$ . Apart from the boundary conditions (5-1) reformulated in the Cartesian coordinate system, the following ones are imposed on the right and bottom edges:

$$u_x(b, y) = 0 \quad (\text{displacement condition}), \quad (5-9a)$$

$$u_y(x, b) = 0 \quad (\text{displacement condition}). \quad (5-9b)$$

It is assumed that  $b = 10a$  to reduce the effect of the boundaries on the elastic field near the loading point. At the same time, the reasonable domain size protects the discrete model from an excessive number of finite elements.

For an efficient mesh generation, a quarter-disc of radius  $2a$ , centered at the origin, is set apart from the whole domain. The defined maximal element size within this subregion is significantly lower than outside. Moreover, taking into account the peak character of the loaded boundary displacement, a nonuniform mesh distribution is applied: mesh density increases towards the loading point. An exemplary fragment of the discretized system  $\widehat{\Omega}$  is shown in Figure 13. The quadratic quadrilateral elements are used in the entire domain.

Figure 14 presents numerical results for  $\nu = 0.25$  and  $\nu = -0.5$  in the nondimensional form: the distribution of displacement  $U_y$  and stress  $S_y$  as well as the vertical displacement of the loaded surface  $-U_y(x, 0)$ . Thus, the graphs correspond to Figure 6 (top/middle left and top/middle right) and Figure 7 (left). The displacement and stress fields produced by two different methods are in close agreement with each other. When it comes to the loaded boundary, the maximal displacements obtained with FEM are

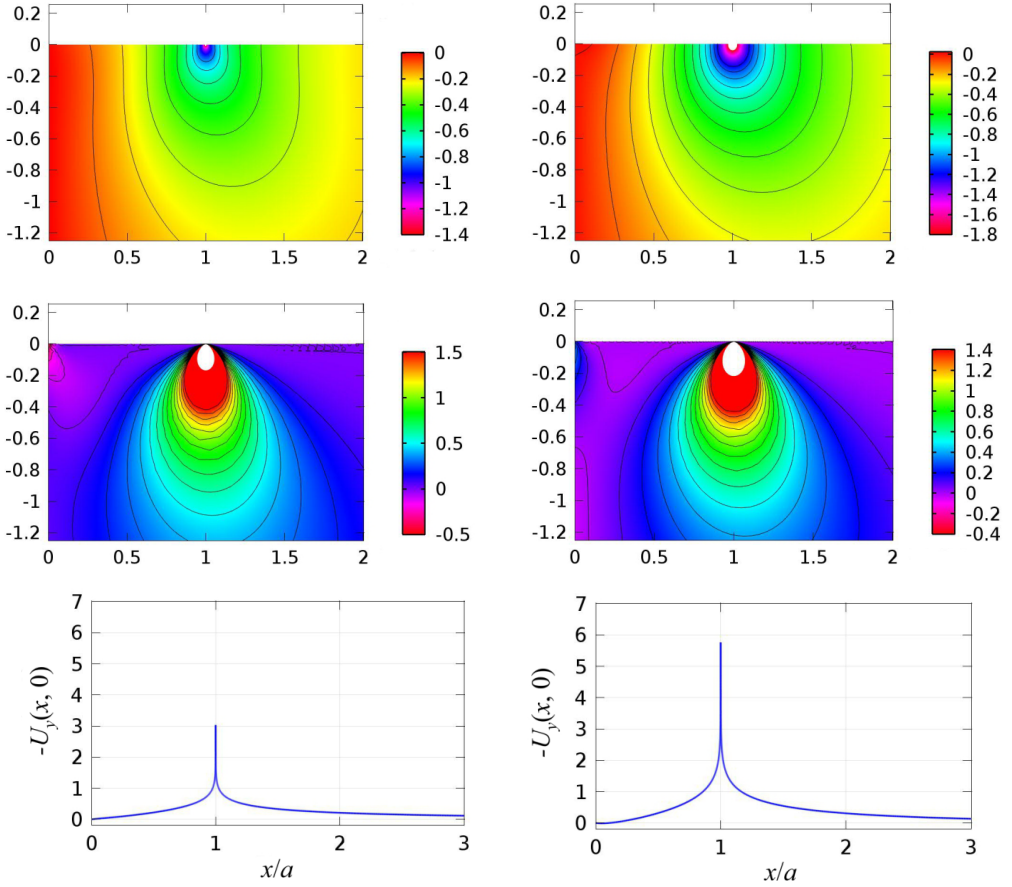


**Figure 14.** Displacement and stress field for  $\nu = 0.25$  (left column) and  $\nu = -0.5$  (right column): (top) normal stress  $S_y$ , (middle) vertical displacement  $U_y$  and (bottom) upward displacement  $-U_y$  of the loaded surface.

2–5% greater than the ones from the semianalytical solutions. The simulations were performed for the number of finite elements  $n_e = 13\,938$  and the number of degrees of freedom  $n_{\text{dof}} = 112\,606$ .

In order to examine the convergence of computations, a series of numerical experiments were conducted for gradually increasing mesh density inside the quarter-disc subdomain. As can be seen in [Figure 15](#), left, a significant growth of the maximal value  $-U_y(a, 0)$  occurs for relatively small numbers of degrees of freedom. Nevertheless, the displacement stabilizes when  $n_{\text{dof}} > 118\,000$ . An analogous test for the semianalytical approach (see [Figure 15](#), right) indicates more regular change of the peak displacement with the number of complex poles  $n_c^*$ : logarithmic convergence rate is clearly observed (notice the logarithmic scale on the horizontal axis).

It should be emphasized that achieving such an agreement between both methods has been somewhat troublesome from the viewpoint of FEM. Using gradually finer but uniform meshes in the whole quarter-disc region does not bring the expected results: the maximal displacement grows much slower than the number of degrees of freedom. Consequently, gaining reliable values becomes unattainable even for

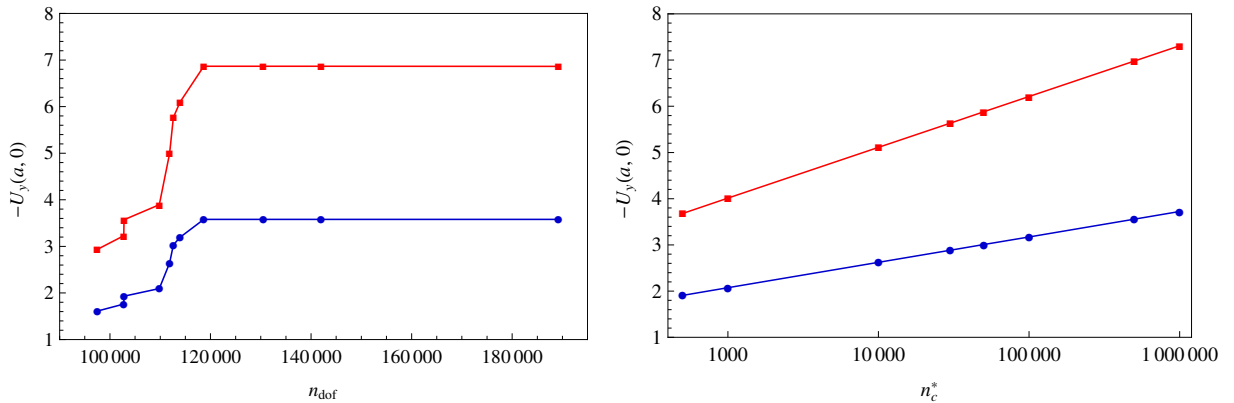


**Figure 15.** Convergence of the maximal vertical displacement for  $\nu = 0.25$  ( $\bullet$ ) and  $\nu = -0.5$  ( $\blacksquare$ ): (left) FEM results and (right) results of the semianalytical approach.

users of PCs with relatively large memory resources. Hence, increasing the mesh density locally (at the loading point) is indispensable.

However, these difficulties and, more generally, the requirement for high-resolution computations by the two methods (large  $n_{\text{dof}}$  and  $n_c^*$ , respectively) relate mainly to a small neighborhood of the loading point. The displacement and stress fields far enough from this point are rather weakly affected by a change in  $n_{\text{dof}}$  and  $n_c^*$ .

A comparison of the curve  $U_\varphi(r, \pi/2)$  from Figure 8 ( $n_c^* = 3 \times 10^4$ ) and the one obtained by FEM ( $n_{\text{dof}} = 112\,606$ ) for  $\nu = -0.75$  is presented in Figure 16. As can be seen, the applied discretization method is sufficient and the results capture the valley effect very well. Noticeable differences appear for  $x/a > 3/2$ , and they grow with increasing  $x$ . However, this discrepancy can be effectively eliminated by adjusting  $n_{\text{dof}}$  and  $n_c^*$  to ensure very close values of the peak displacements  $-U_y(a, 0)$  provided by both approaches.

## 6. Conclusions

In this paper, the distributions of the vertical displacement as well as the normal and shear stresses in a finite subregion of the quarter-plane have been discussed. Much attention has been paid to the deformation of the loaded boundary, which has been analyzed for various values of Poisson's ratio. It has been found that auxetics exhibit an anomalous deformation of the loaded surface near the fixed boundary: the valley effect that intensifies with stronger auxeticity of the material. The obtained results indicate that  $\nu = 0$  is just the critical value below which the effect always occurs. A simple explanation of the unusual deformation mechanism has been suggested by using the example of an unconstrained auxetic and nonauxetic solid under a tensile load. The presented solutions are in close agreement with the FEM results, although the latter ones have been obtained for a finite-sized solid.

The discussed valley effect can be treated as a kind of ersatz of negative stiffness (or negative compliance). In the case of the analyzed system, it arises from a combination of specific conditions: constraints (fixed boundary), load (vertical concentrated force) and material ( $\nu \leq 0$ ). But generally, the systems exhibiting negative stiffness are interesting from both theoretical and practical points of view.

Combining an ordinary material with the one of negative stiffness may produce a composite having amazing properties, e.g., very large elastic modulus. In theory, it is possible to construct a material of zero compliance [Maruszewski et al. 2010; Poźniak et al. 2010]. Such modern trends in science and engineering require efficient numerical simulations that cast new light on unusual phenomena that have not yet been investigated experimentally.

Assuming the semi-infinite character of the domain allows for a semianalytical treatment of the problem. Such an approach has a huge advantage compared to purely numerical techniques. One can focus on the displacement and stress analysis of the loaded surface only, without the necessity of solving the problem in the whole domain. Moreover, the proposed method is free from various difficulties connected to the discretization process. Based on the obtained results, it may be concluded that the semianalytical approach exhibits logarithmic convergence.

### References

- [Alderson and Alderson 2007] A. Alderson and K. L. Alderson, “Auxetic materials”, *J. Aerosp. Eng. (ASCE)* **221**:4 (2007), 565–575.
- [Bai and Lu 2004] F. Bai and W.-Q. Lu, “The selection and assemblage of approximation functions and disposal of its singularity in axisymmetric DRBEM for heat transfer problems”, *Eng. Anal. Bound. Elem.* **28**:8 (2004), 955–965.
- [Bateman 1954] H. Bateman, *Tables of integral transforms, I*, edited by A. Erdélyi et al., McGraw-Hill, New York, 1954.
- [Bronsztajn et al. 2009] I. N. Bronsztajn, K. A. Siemiendajew, G. Musiol, and H. Mühlig, *Nowoczesne kompendium matematyki*, PWN, Warsaw, 2009.
- [Debnath and Bhatta 2007] L. Debnath and D. Bhatta, *Integral transforms and their applications*, 2nd ed., Chapman & Hall/CRC, Boca Raton, FL, 2007.
- [Erdogan and Arin 1976] F. Erdogan and K. Arin, “Fracture and contact problems for an elastic wedge”, *J. Elasticity* **6**:1 (1976), 57–71.
- [Evans and Alderson 2000] K. E. Evans and K. L. Alderson, “Auxetic materials: the positive side of being negative”, *Eng. Sci. Educ. J.* **9**:4 (2000), 148–154.

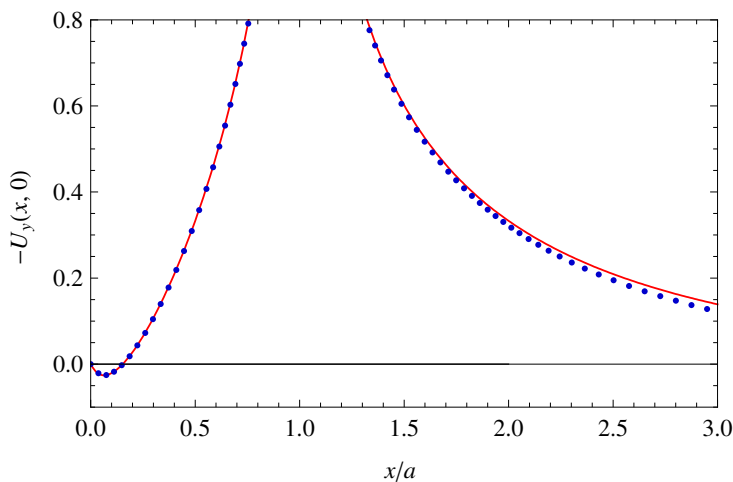


**Figure 16.** The effect of the anomalous vertical displacement of the loaded surface for  $\nu = -0.75$ : results of the semianalytical approach (line) and FEM results (dots).

- [Greaves et al. 2011] G. N. Greaves, A. L. Greer, R. S. Lakes, and T. Rouxel, “Poisson’s ratio and modern materials”, *Nat. Mater.* **10**:11 (2011), 823–837.
- [Johnson 1985] K. L. Johnson, *Contact mechanics*, Cambridge Univ. Press, 1985.
- [Kaplan 2002] W. Kaplan, *Advanced calculus*, 5th ed., Addison-Wesley, Boston, 2002.
- [Kącki 1992] E. Kącki, *Równania różniczkowe cząstkowe w zagadnieniach fizyki i techniki*, 3rd ed., WNT, Warsaw, 1992.
- [Lakes 2001] R. S. Lakes, “Extreme damping in composite materials with a negative stiffness phase”, *Phys. Rev. Lett.* **86**:13 (2001), 2897–2900.
- [Lakes et al. 2001] R. S. Lakes, T. Lee, A. Bersie, and Y. Wang, “Extreme damping in composite materials with negative-stiffness inclusions”, *Nature* **410**:6828 (2001), 565–567.
- [Liu 2010] G. R. Liu, *Meshfree methods: moving beyond the finite element method*, 2nd ed., CRC Press, Boca Raton, FL, 2010.
- [Martin 2003] P. A. Martin, “On Green’s function for a bimaterial elastic half-plane”, *Int. J. Solids Struct.* **40**:9 (2003), 2101–2119.
- [Maruszewski et al. 2010] B. Maruszewski, T. Stręk, A. A. Poźniak, and K. W. Wojciechowski, “Computational modelling of auxetics”, Chapter 12, pp. 265–284 in *Finite element analysis*, edited by D. Moratal, Sciyo, Croatia, 2010.
- [Nowacki 1970] W. Nowacki, *Teoria sprężystości*, PWN, Warsaw, 1970.
- [Poźniak et al. 2010] A. A. Poźniak, H. Kamiński, P. Kędziora, B. Maruszewski, T. Stręk, and K. W. Wojciechowski, “Anomalous deformation of constrained auxetic square”, *Rev. Adv. Mater. Sci.* **23**:2 (2010), 169–174.
- [Prawoto 2012] Y. Prawoto, “Seeing auxetic materials from the mechanics point of view: a structural review on the negative Poisson’s ratio”, *Comput. Mater. Sci.* **58** (2012), 140–153.
- [Saada 1993] A. S. Saada, *Elasticity: theory and applications*, 2nd ed., Krieger, Malabar, FL, 1993.
- [Sadd 2005] M. H. Sadd, *Elasticity: theory, applications, and numerics*, Elsevier, Boston, 2005.
- [Sneddon 1951] I. N. Sneddon, *Fourier transforms*, McGraw-Hill, New York, 1951.
- [Theocaris and Makrakis 1987] P. S. Theocaris and G. Makrakis, “Crack kinking in anti-plane shear solved by the Mellin transform”, *Int. J. Fract.* **34**:4 (1987), 251–262.
- [Timoshenko and Goodier 1951] S. Timoshenko and J. N. Goodier, *Theory of elasticity*, 2nd ed., McGraw-Hill, New York, 1951.
- [Tsamaphyros and Theocaris 1979] G. Tsamaphyros and P. S. Theocaris, “On the solution of the sector problem”, *J. Elasticity* **9**:3 (1979), 271–281.
- [Walczak et al. 2014] T. Walczak, G. Sypniewska-Kamińska, B. T. Maruszewski, and K. W. Wojciechowski, “Mesh versus meshless method of elastic displacement determination in a common and an auxetic material”, *Phys. Status Solidi B* **251**:11 (2014), 2225–2232.

Received 30 Sep 2014. Revised 23 Mar 2015. Accepted 23 Mar 2015.

PAWEŁ FRITZKOWSKI: [pawel.fritzkowski@put.poznan.pl](mailto:pawel.fritzkowski@put.poznan.pl)  
 Institute of Applied Mechanics, Poznań University of Technology, Jana Pawła II 24, 60-965 Poznań, Poland

HENRYK KAMIŃSKI: [henryk.kaminski@put.poznan.pl](mailto:henryk.kaminski@put.poznan.pl)  
 Institute of Applied Mechanics, Poznań University of Technology, Jana Pawła II 24, 60-965 Poznań, Poland

# JOURNAL OF MECHANICS OF MATERIALS AND STRUCTURES

[msp.org/jomms](http://msp.org/jomms)

Founded by Charles R. Steele and Marie-Louise Steele

## EDITORIAL BOARD

ADAIR R. AGUIAR	University of São Paulo at São Carlos, Brazil
KATIA BERTOLDI	Harvard University, USA
DAVIDE BIGONI	University of Trento, Italy
YIBIN FU	Keele University, UK
IWONA JASIUK	University of Illinois at Urbana-Champaign, USA
C. W. LIM	City University of Hong Kong
THOMAS J. PENCE	Michigan State University, USA
DAVID STEIGMANN	University of California at Berkeley, USA

## ADVISORY BOARD

J. P. CARTER	University of Sydney, Australia
D. H. HODGES	Georgia Institute of Technology, USA
J. HUTCHINSON	Harvard University, USA
D. PAMPLONA	Universidade Católica do Rio de Janeiro, Brazil
M. B. RUBIN	Technion, Haifa, Israel

**PRODUCTION** [production@msp.org](mailto:production@msp.org)

SILVIO LEVY Scientific Editor

Cover photo: Ev Shafrir

---

See [msp.org/jomms](http://msp.org/jomms) for submission guidelines.


---

JoMMS (ISSN 1559-3959) at Mathematical Sciences Publishers, 798 Evans Hall #6840, c/o University of California, Berkeley, CA 94720-3840, is published in 10 issues a year. The subscription price for 2016 is US\$575/year for the electronic version, and \$735/year (+\$60, if shipping outside the US) for print and electronic. Subscriptions, requests for back issues, and changes of address should be sent to MSP.

---

JoMMS peer-review and production is managed by EditFLOW<sup>®</sup> from Mathematical Sciences Publishers.

PUBLISHED BY

 **mathematical sciences publishers**  
nonprofit scientific publishing

<http://msp.org/>

© 2016 Mathematical Sciences Publishers

## Special issue

### Trends in Continuum Physics (TRECOP 2014)

<b>Preface</b>	<b>BOGDAN T. MARUSZEWSKI, WOLFGANG MUSCHIK, ANDRZEJ RADOWICZ and KRZYSZTOF W. WOJCIECHOWSKI</b>	<b>1</b>
<b>Stress and displacement analysis of an auxetic quarter-plane under a concentrated force</b>	<b>PAWEŁ FRITZKOWSKI and HENRYK KAMIŃSKI</b>	<b>3</b>
<b>Laminar flow of a power-law fluid between corrugated plates</b>	<b>JAKUB KRZYSZTOF GRABSKI and JAN ADAM KOŁODZIEJ</b>	<b>23</b>
<b>A study of elastic-plastic deformation in the plate with the incremental theory and the meshless methods</b>	<b>MALGORZATA A. JANKOWSKA and JAN ADAM KOŁODZIEJ</b>	<b>41</b>
<b>Implementation of HAM and meshless method for torsion of functionally graded orthotropic bars</b>	<b>ANITA UŚCIEŁOWSKA and AGNIESZKA FRASKA</b>	<b>61</b>
<b>The application of the method of fundamental solutions in modeling auxetic materials</b>	<b>TOMASZ WALCZAK, GRAZYNA SYPNIEWSKA-KAMIŃSKA, BOGDAN T. MARUSZEWSKI and KRZYSZTOF W. WOJCIECHOWSKI</b>	<b>79</b>